ELSEVIER

Physica A 255 (1998) 221–241

PHYSICA A

Three-dimensional local porosity analysis of porous media

B. Biswal[a,b], C. Manwart[a], R. Hilfer[a,c]

[a] *ICA-1, Universität Stuttgart, Pfaffenwaldring 27, 70569 Stuttgart, Germany*
[b] *Department of Physics & Electronics, Sri Venkateswara College, University of Delhi, New Delhi 110 021, India*
[c] *Institut für Physik, Universität Mainz, 55099 Mainz, Germany*

Received 5 February 1998

Abstract

A quantitative comparison of the pore space geometry for three natural sandstones is presented. The comparison is based on local porosity theory which provides a geometric characterization of stochastic microstructures. The characterization focusses on porosity and connectivity fluctuations. Porosity fluctuations are measured using local porosity distributions while connectivity fluctuations are measured using local percolation probabilities. We report the first measurement of local percolation probability functions for experimentally obtained three-dimensional pore space reconstructions. Our results suggest the use of local porosity distributions and percolation probabilities as a quantitative method to compare microstructures of models and experiment. © 1998 Published by Elsevier Science B.V. All rights reserved

PACS: 61.43.G; 81.05.Rm; 47.55.Mh
Keywords: Porous materials; Structure; Granular materials; Flows through porous media

---

1. Introduction

A large number of microscopic models have been proposed to represent the microstructure of porous media [1–12]. Representative microscopic models are a prerequisite for studying transport properties such as fluid flow or sound propagation in oil reservoirs, aquifers or other random media.

Microscopic models are not unique, and hence it is necessary to have criteria for comparing them among each other and with the experimental porous microstructure [13–17]. This is particularly important for attempts to generate porous microstructures

0378-4371/98/$19.00 Copyright © 1998 Published by Elsevier Science B.V. All rights reserved
PII S0378-4371(98)00111-3

in an automatic computerized process [18,7,8,19], or to decide quantitatively whether the connectivity is percolationlike as is often assumed in models [20,21,11].

Detailed microscopic models contain so many geometrical features that a rough comparison based only on porosity and specific surface is insufficient. The problem is to find general geometric characterization methods to test how well a model represents the microstructure found in reality. Given such tools they can then be used to constrain the input parameters of the models.

General geometric characterization methods traditionally employ only porosities, specific surface areas, and sometimes correlation functions [2,22,23,7,24]. Recently, novel tools based on local porosity theory became available for the comparison of stochastic microstructures [25–27,13,28–30,15]. Local porosity theory is currently the most general geometric characterization method because it contains as a special case also the characterization through correlation functions (see [15] for details).

Local porosity theory contains two geometric characteristics. The first is local porosity distributions, the second is local percolation probabilities [15]. While local porosity distributions have been measured previously on artificial and real samples [13,29–31] no reliable measurement has been made up to now for the local percolation probabilities. The main impediment has been the absence of accurate three-dimensional pore space representations for real rocks.

The objective of the work reported here was to measure the local percolation probabilities of natural sandstones thereby providing a new geometric characteristic against which microscopic pore space models can be compared [35].

2. Measured quantities

2.1. Local porosity distributions

Local porosity distributions were originally introduced as a quantitative substitute for pore size distributions [25]. The idea is to measure porosity or other well-defined geometric observables within a bounded (compact) subset of the porous medium and to collect these measurements into various histograms (empirical probability densities).

Imagine a porous medium occupying a subset $\mathbb{S} \subset \mathbb{R}^d$ of the physical space ($d = 3$ in the following). For the data analysed here the set $\mathbb{S}$ is a rectangular parallelepiped whose sidelengths are M_1, M_2 and M_3 in units of the lattice constant a (resolution) of a simple cubic lattice. The sample $\mathbb{S}$ contains two disjoint subsets $\mathbb{S} = \mathbb{P} \cup \mathbb{M}$ with $\mathbb{P} \cap \mathbb{M} = \emptyset$ where $\mathbb{P}$ is the pore space and $\mathbb{M}$ is the rock or mineral matrix and $\emptyset$ is the empty set. In practice, the sample is discretized, and the configuration of the two sets $\mathbb{P}$ and $\mathbb{M}$ is given as an $M_1 \times M_2 \times M_3$-array of two numbers representing $\mathbb{P}$ and $\mathbb{M}$, respectively. Let $\mathbb{K}(\mathbf{x}, L)$ denote a cube of sidelength L centred at the lattice vector $\mathbf{x}$. The set $\mathbb{K}(\mathbf{x}, L)$ defines a measurement cell inside of which local geometric properties such as porosity or specific internal surface are measured. The local porosity in this measurement cell $\mathbb{K}(\mathbf{x},L)$ is defined as

$$\phi(\mathbf{x},L)=\frac{V(\mathbb{P}\cap\mathbb{K}(\mathbf{x},L))}{V(\mathbb{K}(\mathbf{x},L))}\,, \tag{2.1}$$

where $V(\mathbb{G})$ is the volume of the set $\mathbb{G}\subset\mathbb{R}^d$. The local porosity distribution $\mu(\phi,L)$ is defined as

$$\mu(\phi,L)=\frac{1}{m}\sum_{\mathbf{x}}\delta(\phi-\phi(\mathbf{x},L))\,, \tag{2.2}$$

where m is the number of placements of the measurement cell $\mathbb{K}(\mathbf{x},L)$. The results presented below are obtained by placing $\mathbb{K}(\mathbf{x},L)$ on all lattice sites $\mathbf{x}$ which are at least a distance $L/2$ from the boundary of $\mathbb{S}$, and hence in the following:

$$m=\prod_{i=1}^{3}(M_i-L+1) \tag{2.3}$$

will be used. $\mu(\phi,L)$ is the empirical probability density function (histogram) of local porosities. Its support is the unit interval.

It is simple to determine $\mu(\phi,L)$ in the limits $L\to 0$ and $L\to\infty$ of small and large measurement cells. For small cells one finds generally [25,15]

$$\mu(\phi,L=0)=\bar{\phi}\delta(\phi-1)+(1-\bar{\phi})\delta(\phi)\,, \tag{2.4}$$

where

$$\bar{\phi}=V(\mathbb{P}\cap\mathbb{S})/V(\mathbb{S}) \tag{2.5}$$

is the bulk porosity. If the sample is macroscopically homogeneous then

$$\mu(\phi,L\to\infty)=\delta(\phi-\bar{\phi}) \tag{2.6}$$

indicating that in both limits the geometrical information contained in $\mu(\phi,L)$ consists of the single number $\bar{\phi}$. The macroscopic limit, however, involves the question of macroscopic heterogeneity versus macroscopic homogeneity (for more information see [15]). In any case, if Eqs. (2.4) and (2.6) hold, it follows that there exists a special length scale L^* defined as

$$L^*=\min\{L\colon\ \mu(0,L)=\mu(1,L)=0\}\,, \tag{2.7}$$

at which the δ-distributions at $\phi=0$ and 1 both vanish for the first time.

2.2. Local percolation probabilities

The local percolation probabilities characterize the connectivity of measurement cells of a given local porosity. Let

$$\Lambda_\alpha(\mathbf{x},L)=\begin{cases}1 & \text{if } \mathbb{K}(\mathbf{x},L) \text{ percolates in “}\alpha\text{”-direction,}\\ 0 & \text{otherwise}\end{cases} \tag{2.8}$$

Table 1
Legend for index α of local percolation probabilities $\lambda_\alpha(\phi, L)$

Index α	Meaning
x	x-direction
y	y-direction
z	z-direction
3	$(x \wedge y \wedge z)$-direction
c	$(x \vee y \vee z)$-direction
0	$(\neg(x \vee y \vee z))$-direction

be an indicator for percolation. What is meant by "α"-direction is summarized in Table 1.

A cell $\mathbb{K}(\mathbf{x}, L)$ is called "percolating in the x-direction" if there exists a path inside the set $\mathbb{P} \cap \mathbb{K}(\mathbf{x}, L)$ connecting those two faces of $\mathbb{S}$ that are vertical to the x-axis. Similarly for the other directions. Thus, $\Lambda_3 = 1$ indicates that the cell can be traversed along all three directions, while $\Lambda_c = 1$ indicates that there exists at least one direction along which the block is percolating. $\Lambda_0 = 1$ indicates a blocking cell.

The local percolation probability in the "α"-direction is now defined through

$$\lambda_\alpha(\phi, L) = \frac{\sum_{\mathbf{x}} \Lambda_\alpha(\mathbf{x}, L)\delta_{\phi\phi(\mathbf{x}, L)}}{\sum_{\mathbf{x}} \delta_{\phi\phi(\mathbf{x}, L)}} . \tag{2.9}$$

The local percolation probability $\lambda_\alpha(\phi, L)$ gives the fraction of measurement cells of sidelength L with local porosity ϕ that are percolating in the "α"-direction.

2.3. Total fraction of percolating cells

The total fraction of all cells percolating along the "α"-direction is given by integration over all local porosities as

$$p_\alpha(L) = \int_0^1 \mu(\phi, L)\lambda_\alpha(\phi, L)\, d\phi . \tag{2.10}$$

This quantitiy provides an important characteristic for network models. For a network model it gives the fraction of network elements (bond, sites, etc.) which have to be permeable.

3. Samples and algorithms

The data sets of three different sandstones are used in the analysis below. Each data set consists of a three-dimensional array of 0's and 1's indicating pore space $\mathbb{P}$ or matrix $\mathbb{M}$. The array dimensions are M_1, M_2 and M_3. The pore space $\mathbb{P}$ of the

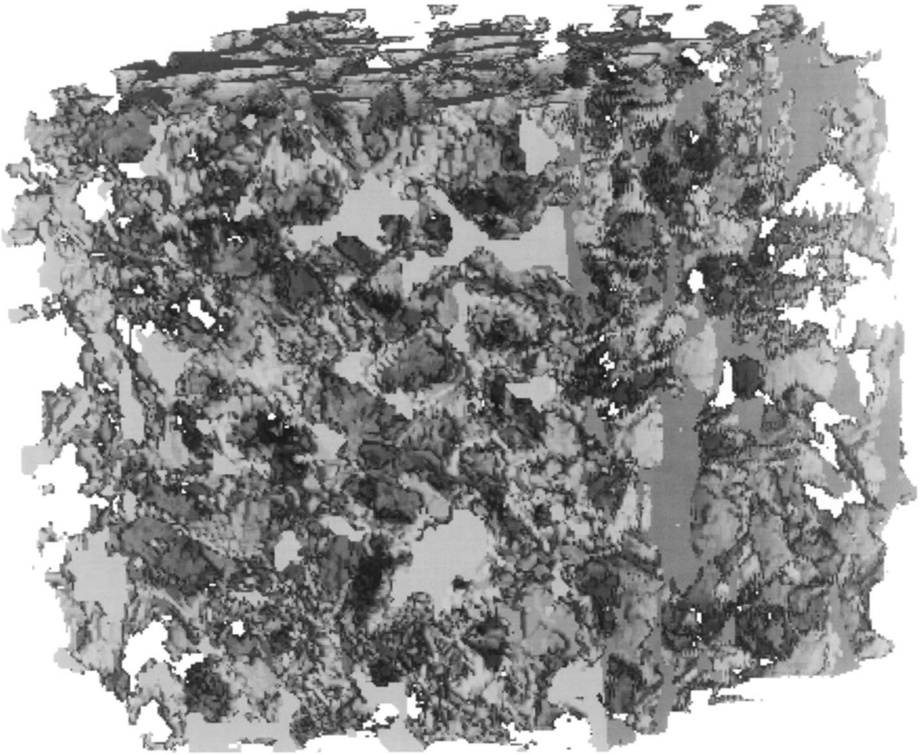

Fig. 1. Three-dimensional pore space of Berea sandstone (sample A). The resolution is $a = 10\,\mu\text{m}$, the sample dimensions are $M_1 = 128$, $M_2 = 128$, $M_3 = 128$. The bulk porosity is $\bar{\phi} = 0.1775$. The pore space is indicated in grey, the matrix space is transparent.

Table 2
Overview over properties of the data sets for three reservoir sandstones

Sample	Description	a (μm)	$M_1 \times M_2 \times M_3$	L^* (μm)	$\bar{\phi}$	$\bar{k}$ (mD)
A	Berea	10	$128 \times 128 \times 128$	260	0.1775	1100
B	Brent	2.7	$180 \times 217 \times 217$	108	0.1602	470
C	Sst20d	30	$73 \times 128 \times 128$	540	0.2470	20 000

three samples are displayed in Figs. 1, 2 and 3. Note that the representations are not to scale because the resolution of each image is different. The data were obtained by computerized microtomography [32].

Table 2 gives a synopsis of the characteristics of the three samples which have been analysed. Here a is the resolution, and M_i are the dimensionless sidelengths of the sample in units of a. The bulk porosity was defined in Eq. (2.5) and the length L^* in Eq. (2.7). The permeability $\bar{k}$, given in millidarcy, is the experimentally determined permeability of the sample from which the data sets were obtained.

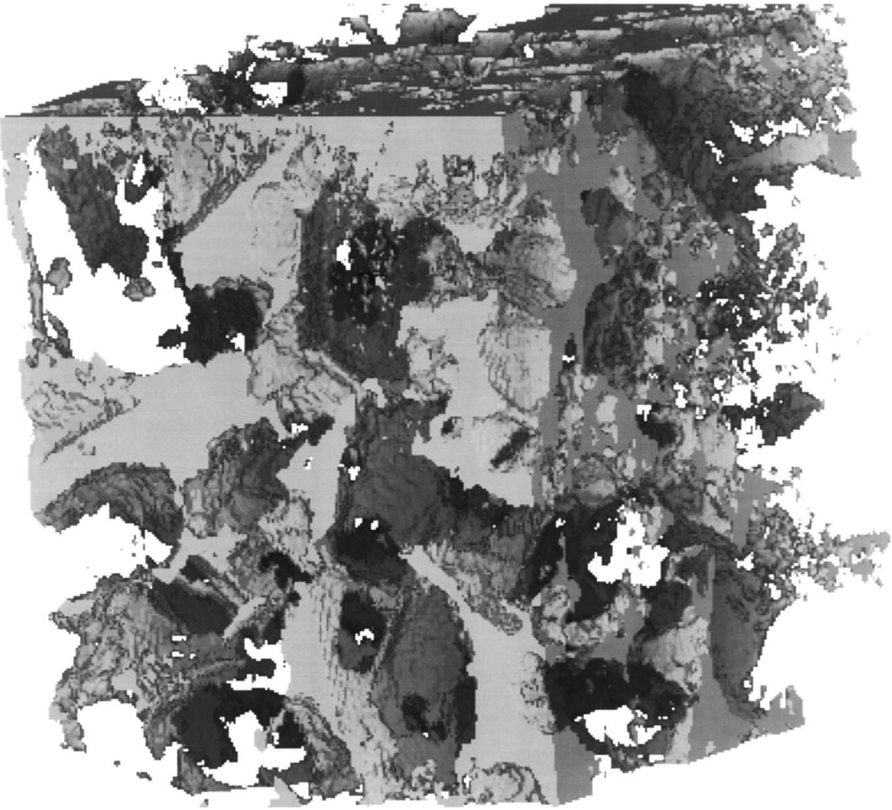

Fig. 2. Three-dimensional pore space reconstruction of Brent sandstone (sample B). The resolution is $a = 2.7\,\mu\text{m}$, the sample dimensions are $M_1 = 180$, $M_2 = 217$, $M_3 = 217$. The bulk porosity is $\bar{\phi} = 0.1602$. The pore space is indicated in grey, the matrix space is transparent.

The calculation of $\mu(\phi, L)$ is straightforward, and proceeds exactly according to Eq. (2.2). Several possibilities exist for the choice of $\mathbf{x}$ in $\mathbb{K}(\mathbf{x}, L)$. Originally [25], it was proposed to choose for $\mathbf{x}$ a cubic lattice with lattice constant L such that $\bigcup_{\mathbf{x}} \mathbb{K}(\mathbf{x}, L) = \mathbb{S}$ and such that the resulting set of $\mathbb{K}(\mathbf{x}, L)$ are nonoverlapping, i.e. $\mathbb{K}(\mathbf{x}, L) \cap \mathbb{K}(\mathbf{x}', L) = \emptyset$ for $\mathbf{x} \neq \mathbf{x}'$. For the small data sets available this leads to poor statistics with strong fluctuations in all results. Therefore, we use here a cubic lattice with smaller lattice constants giving rise to overlapping cells. The results below were obtained by using unit lattice constant. In other words, we used for $\mathbf{x}$ all lattice sites except those whose distance from the sample boundary is less than $L/2$. It must be noted, however, that this method of positioning the cells gives progressively higher weight to the central region of the sample. This can, for large L, lead to small differences (roughly 0.005 in the present case) between the bulk porosity $\bar{\phi}$ as defined in Eq. (2.5) and expected local porosity defined as $\int \phi \mu(\phi)\, d\phi$.

The determination of $\Lambda_\alpha(\mathbf{x}, L)$, i.e. of whether or not a cell is percolating in a given direction, was carried out according to the well-known Hoshen–Kopelman algorithm

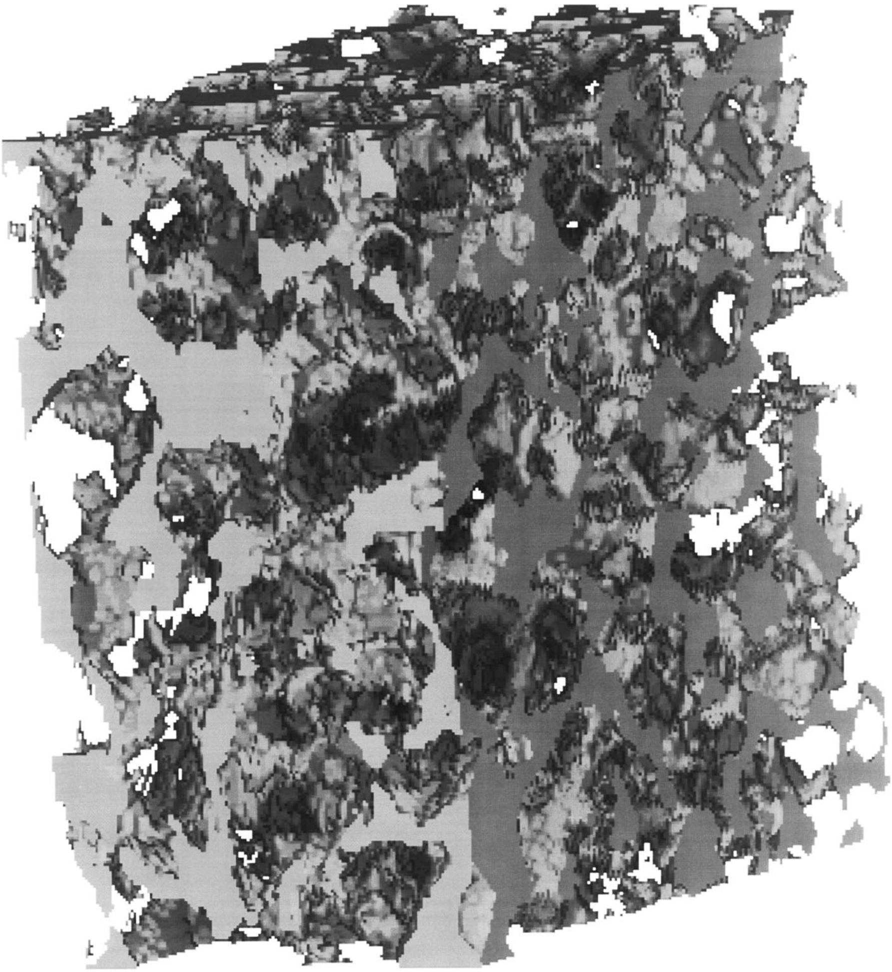

Fig. 3. Three-dimensional pore space reconstruction of a weakly consolidated sandstone (sample C). The resolution is $a = 30\,\mu\text{m}$, the sample dimensions are $M_1 = 73$, $M_2 = 128$, $M_3 = 128$. The bulk porosity is $\bar{\phi} = 0.2450$. The pore space is indicated in grey, the matrix space is transparent.

[33]. The choice of $\mathbf{x}$ was the same as in the measurement of μ. $\lambda_\alpha(\phi, L)$ was then calculated from Eq. (2.9).

4. Results

The first sample is Berea sandstone whose pore space is displayed in Fig. 1. In this case the resolution is $a = 10\,\mu\text{m}$, and the sidelengths of the sample are $M_1 = M_2 = M_3 = 128$. Fig. 4 shows the local porosity distributions $\mu(\phi, L)$ with $L = 40, 80, 120, 300\,\mu\text{m}$ exhibiting the typical crossover between the limits $L = 0$ and ∞. The curves are shown as dotted lines and marked by four different symbols corresponding to the four values of

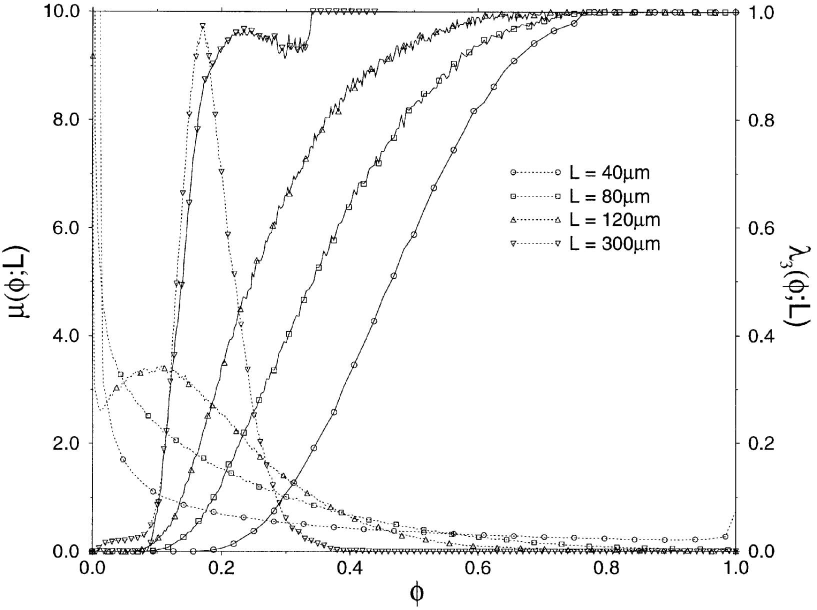

Fig. 4. Local porosity distributions $\mu(\phi,L)$ (dotted lines) and local percolation probabilities $\lambda_3(\phi,L)$ (solid lines) for Berea sandstone (sample A, cf. Fig. 1). Four different values for L are indicated by different symbols defined in the legend. The ordinate for the graphs of $\mu(\phi,L)$ is on the left, the ordinate for $\lambda_3(\phi,L)$ is on the right as indicated by the axis labels.

L as indicated in the legend. Next, in the same Fig. 4, the local percolation probabilities $\lambda_3(\phi,L)$ are displayed for the same four values of L that were used for μ. The curves for $\lambda_3(\phi,L)$ are distinguished from those for $\mu(\phi,L)$ by a solid line style. The symbols used to indicate L are the same in both cases. The ordinate for the λ_3-graphs is the right axis, those for μ-graphs is the left axis. The local percolation probabilities λ_3 are increasing from zero to one. This expresses the fact that the full sample is connected. For $L=40\,\mu\text{m}=4a$ the sidelength of the measurement cell corresponds to four voxels. To have a conducting path in all three directions one needs at least 10 voxels of pore space. This amounts to a porosity of roughly 0.16, and hence all curves $\lambda_3(\phi,4a)$ must vanish below $\phi\approx 0.16$. Similarly, to disconnect at least one of the three directions one needs at least 16 voxels filling a plane. Hence, the curves $\lambda_3(\phi,4a)$ must equal unity above $\phi\approx 1-0.25=0.75$. This can be observed in Fig. 4 for Berea and in Figs. 8 and 11 for the other samples. For general L and dimension d the same consideration gives that λ_3 vanishes below $(dL-d+1)/L^d$ and equals unity above $1-1/L$.

It is instructive to compare μ with λ at a fixed L by superposing them in the same plot. Such a plot is shown in Fig. 5 for $L=L^*$. The characteristic length L^* was defined in Eq. (2.7). For sample A (Berea) its value is found to be $L^*=260\,\mu\text{m}$. To facilitate comparison the local porosity distribution $\mu(\phi,L^*)$ has been rescaled such that its maximum equals unity. All six local percolation functions λ_α are displayed in Fig. 5. The sample appears to be isotropic because the three functions $\lambda_x,\lambda_y,\lambda_z$ all fall

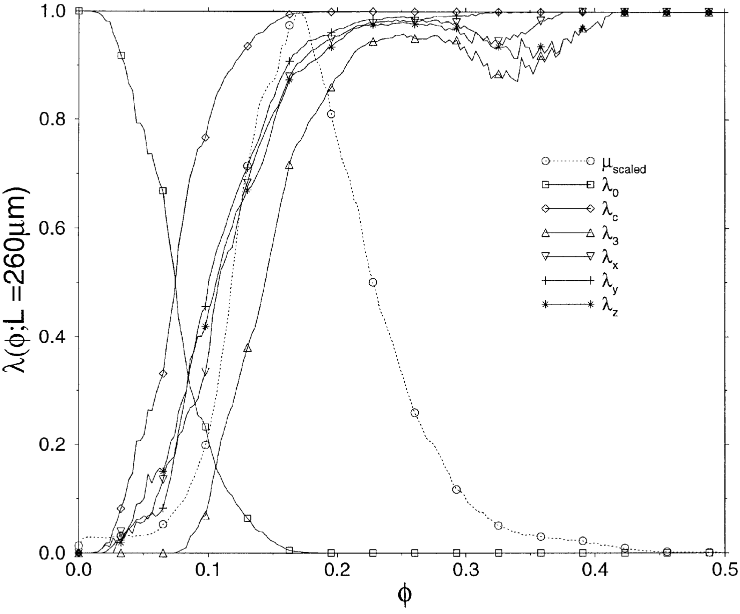

Fig. 5. Local percolation probabilities $\lambda_\alpha(\phi, L^*)$ with $\alpha = 0, 3, c, x, y, z$ and $L^* = 260\,\mu\mathrm{m}$ for Berea sandstone (sample A) shown in Fig. 1. The dotted curve with circular symbols is the local porosity distribution at $L = L^* = 260\,\mu\mathrm{m}$ rescaled to have maximum 1.

on top of each other. The curves λ_c and λ_3 are upper and lower bounds for the region inside which the connectivity increases from "blocking" to "fully connecting". Note also that this band is shifted to the left of the maximum of μ indicating that Berea sandstone is well connected. In fact, the figure shows that an average cell (i.e. a cell with local porosity around 0.18) is percolating with probability larger than 0.75. Only cells with local porosity much below average are blocking.

To investigate how heterogeneities in the connectivity are reflected in the local percolation probabilities, we have constructed an artificial modification of the Berea sample. To this end we have blocked roughly 1200 additional voxels out of the total of $128^3 \approx 2 \times 10^6$ voxels by blocking a plane of $1 \times 100 \times 100$ voxels inside the sample. The orientation of the blocked plane was chosen perpendicular to the x-direction, and the plane was centred in the y- and z-directions. It was placed in the middle, i.e. into the 64th layer along the x-direction. This amounts to a small decrease of porosity by roughly 0.00058. Note that the plane does not block the x-connectivity completely, but leaves an open shell at the sample boundary. The resulting modified porous microstructure was visually indistinguishable from the unmodified one from the perspective of Fig. 1. Only when viewing the sample at right angles from the y- or z-direction it was possible to detect a small modification. In Fig. 6 we display the same superposition of μ and λ for the partially modified sample that was shown in Fig. 5 for the unmodified sample. The local porosity distribution of the partially x-blocked sample is almost identical to that of the unmodified sample. This remains true for all values of L,

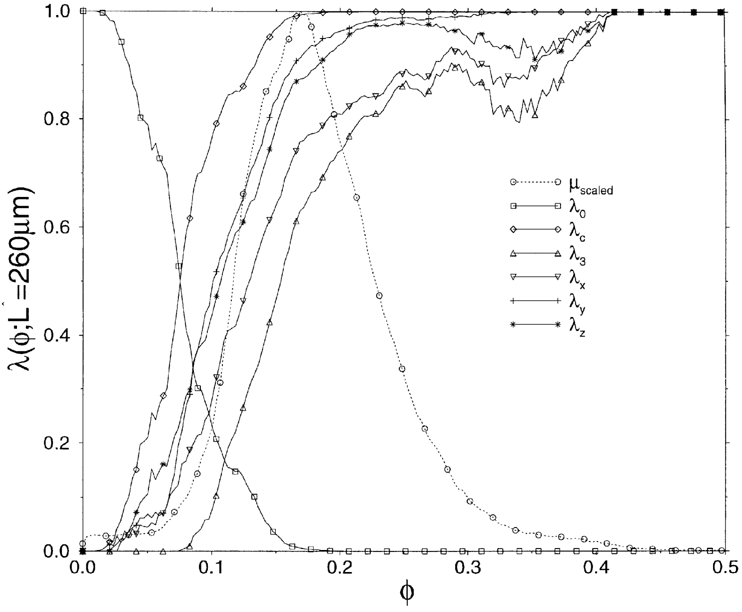

Fig. 6. Same as Fig. 5 but for sample A modified with partially blocking plane in x-direction. See text for details.

and $L^* = 260\,\mu\text{m}$ is also unchanged. The functions $\lambda_0, \lambda_c, \lambda_y$ and λ_z also remain almost unchanged. λ_x, however, differs from λ_y and λ_z as expected. Also, as a consequence, λ_3 falls significantly below the result of the unmodified sample. The deviations of roughly 15% give an order of magnitude for the influence of connectivity fluctuations on λ_3. The difference between the results grows with increasing L. This allows another important conclusion. To characterize heterogeneities using local porosity analysis it is necessary to measure both μ and λ as functions of L over a sufficiently wide range of L. Choosing only one fixed L may be misleading.

The dependence of the difference between the unmodified Berea and the partially blocked sample on L has been further quantified in Fig. 7. This figure shows the total fraction of percolating cells determined according to Eq. (2.10). The results for the original unmodified sample are shown with solid lines, those for the sample with a partially blocking plane are shown as dotted lines. This plot shows again that the unmodified sample is very isotropic because p_x, p_y, p_z overlap. In the partially blocked sample, however, deviations start to appear around $L = 150\,\mu\text{m}$ in $p_x(L)$ and $p_3(L)$ becoming more pronounced at higher L. Note that the modified sample shows a decrease in $p_x(L)$ at $L \approx 300\,\mu\text{m}$ while all curves for the unmodified sample are monotonously increasing. Of course, $p_x(L)$ must start to increase again at $L \gg 400\,\mu\text{m}$ because the sample is still connected on large scales. Therefore, one expects that nonmonotonous behaviour of $p(L)$ correlates with the length scale of heterogeneities in the connectivity.

The next sample is Brent sandstone, shown in Fig. 2, with a resolution of $a = 2.7\,\mu\text{m}$, and sample dimensions $M_1 = 180$, $M_2 = 217$, $M_3 = 217$. Although the data set for this

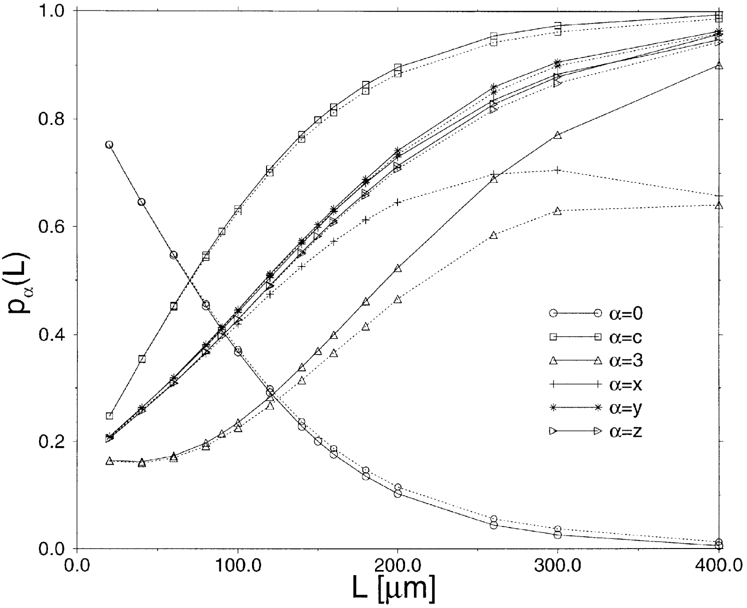

Fig. 7. Total fraction of percolating cells $p_\alpha(L)$ with $\alpha = 0, 3, c, x, y, z$ for Berea sandstone (sample A, cf. Fig. 1) shown as solid lines, and for the modified sample A (with partially blocking *yz*-plane) shown as dotted lines.

sample is the largest one with respect to the number of voxels, its absolute size is the smallest of all samples. As a consequence, the statistics of this sample is poor because it represents little more than a few pores. A larger sample seems necessary to obtain a representative sampling of the pore space.

The local porosity distribution and local percolation probabilities for this sample are shown in Fig. 8 using the same method of plotting as in Fig. 4 (see above). The superposition of $\mu(\phi, L^*)$ and $\lambda(\phi, L^*)$ is displayed in Fig. 9. Finally, the total fraction of percolating cells is shown in Fig. 10. This curve seems to indicate that, while the sample is isotropic for small L, it shows increasing anisotropy at larger L. This effect may, however, also be due to the poor statistics as a result of the small absolute size of the system.

Sample C is a clean weakly consolidated sandstone of unkown origin denoted below as *Sst20d* because its permeability is 20 D. The sample has resolution $a = 30\,\mu\text{m}$ and sample dimensions $M_1 = 73$, $M_2 = 128$, $M_3 = 128$, and its pore space is displayed in Fig. 3. The local porosity distribution for this sample is shown in Fig. 11 together with local percolation probabilities. Their superposition for $L = L^*$ is displayed in Fig. 12. Finally, the total fraction of percolating cells is shown in Fig. 13.

Figs. 12 and 13 indicate that the sample is anisotropic because λ_x is significantly smaller than λ_y and λ_z. It has been checked that this is not a finite size effect due to the sidelength in the x-direction being shorter in this sample than, say, in sample A. This check was carried out by first dividing sample A in half along the x-direction,

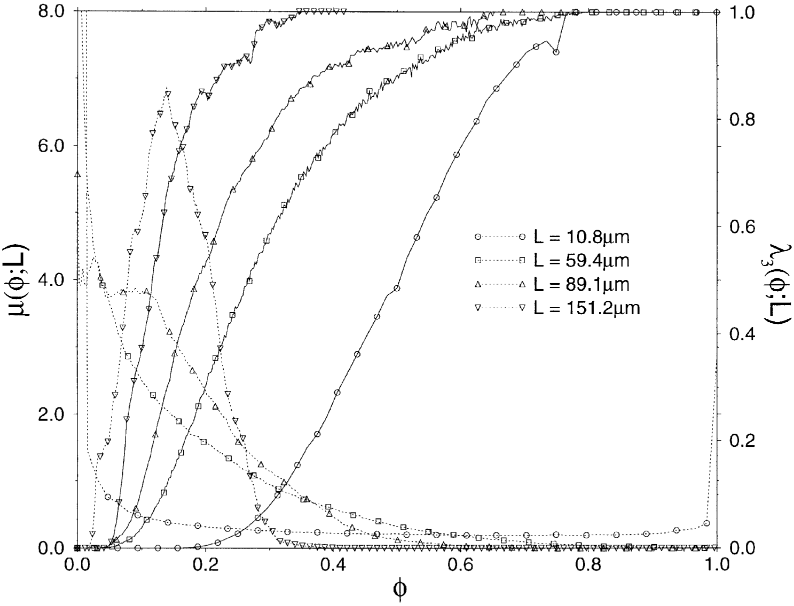

Fig. 8. Local porosity distributions $\mu(\phi,L)$ (dotted lines) and local percolation probabilities $\lambda_3(\phi,L)$ (solid lines) for Brent sandstone (sample B) shown in Fig. 2. Four different values for L are indicated by different symbols defined in the legend. The ordinate for the graphs of $\mu(\phi,L)$ is on the left, the ordinate for $\lambda_3(\phi,L)$ is on the right as indicated by the axis labels.

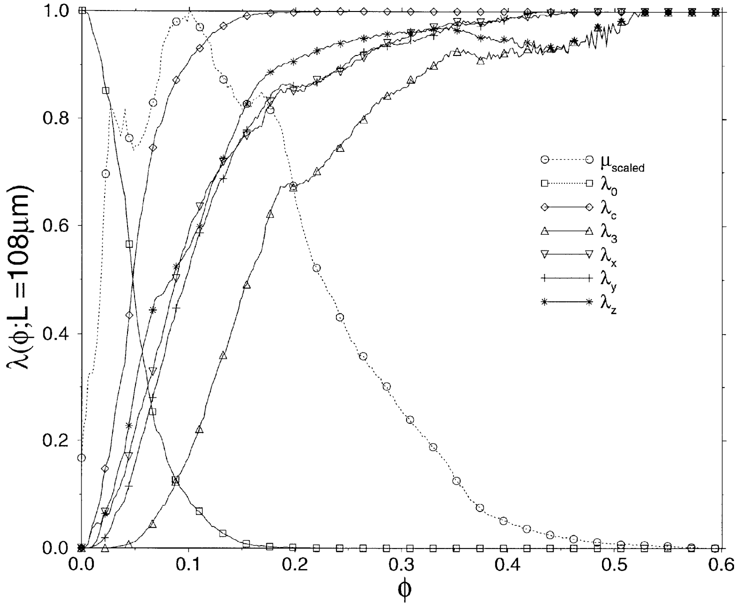

Fig. 9. Local percolation probabilities $\lambda_\alpha(\phi,L^*)$ with $\alpha=0,3,c,x,y,z$ and $L^*=108\,\mu\text{m}$ for Brent sandstone (sample B) shown in Fig. 2. The dotted curve with circular symbols is the local porosity distribution at $L=L^*=108\,\mu\text{m}$ rescaled to have maximum 1.

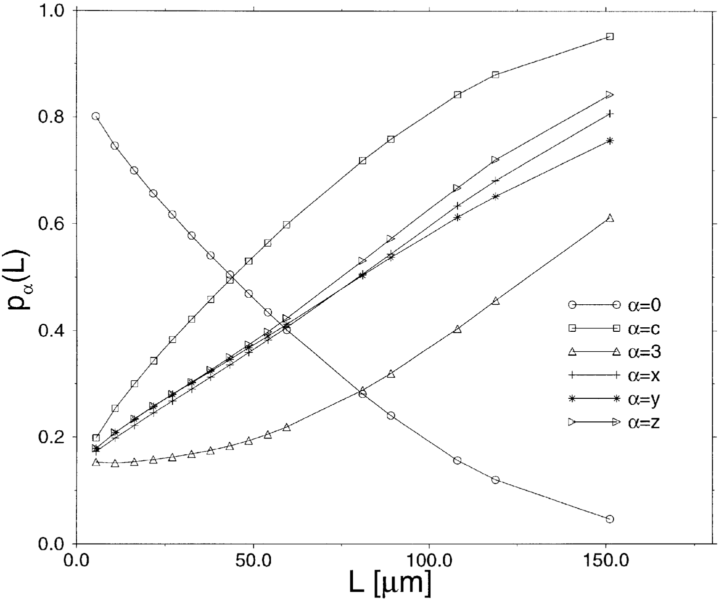

Fig. 10. Total fraction of percolating cells $p_\alpha(L)$ with $\alpha = 0, 3, c, x, y, z$ for Brent sandstone (sample B) shown in Fig. 2.

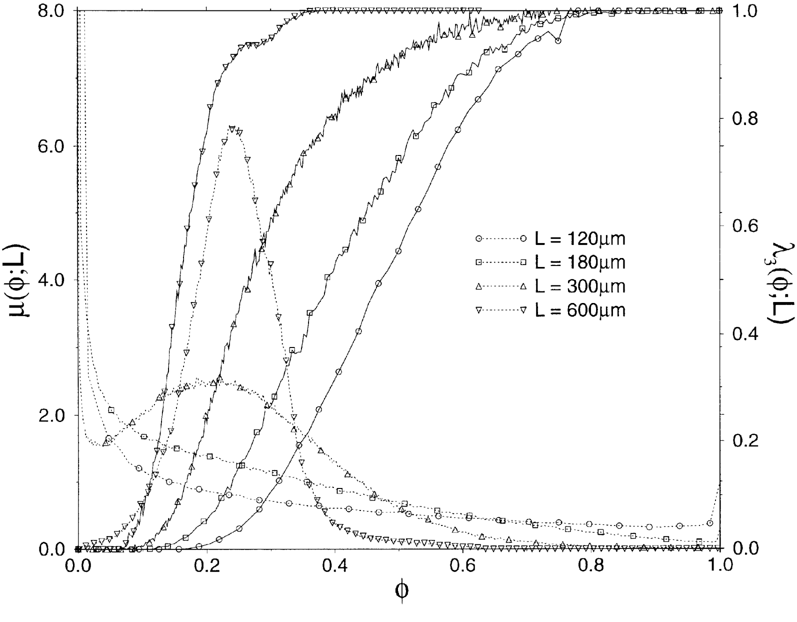

Fig. 11. Local porosity distributions $\mu(\phi, L)$ (dotted lines) and local percolation probabilities $\lambda_3(\phi, L)$ (solid lines) for the sandstone (sample C) shown in Fig. 3. Four different values for L are indicated by different symbols defined in the legend. The ordinate for the graphs of $\mu(\phi, L)$ is on the left, the ordinate for $\lambda_3(\phi, L)$ is on the right as indicated by the axis labels.

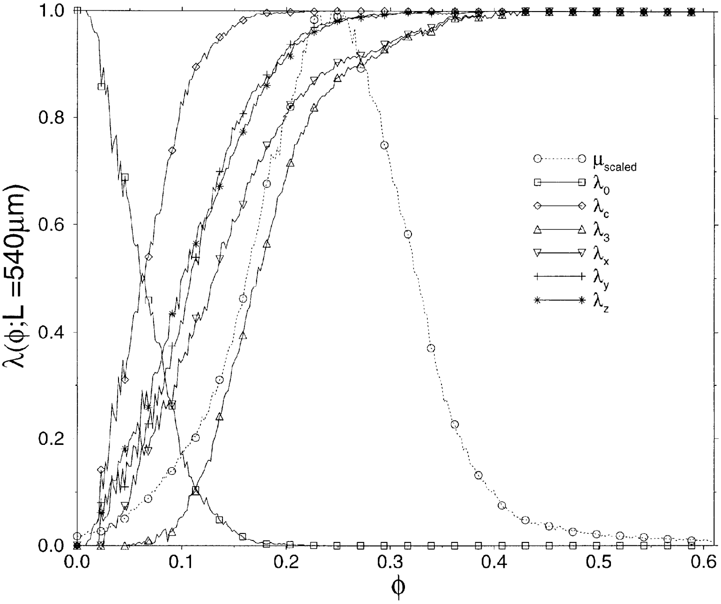

Fig. 12. Local percolation probabilities $\lambda_\alpha(\phi, L)$ superposed on local porosity distribution at $L = L^* = 504\,\mu\mathrm{m}$ for the sandstone shown in Fig. 3.

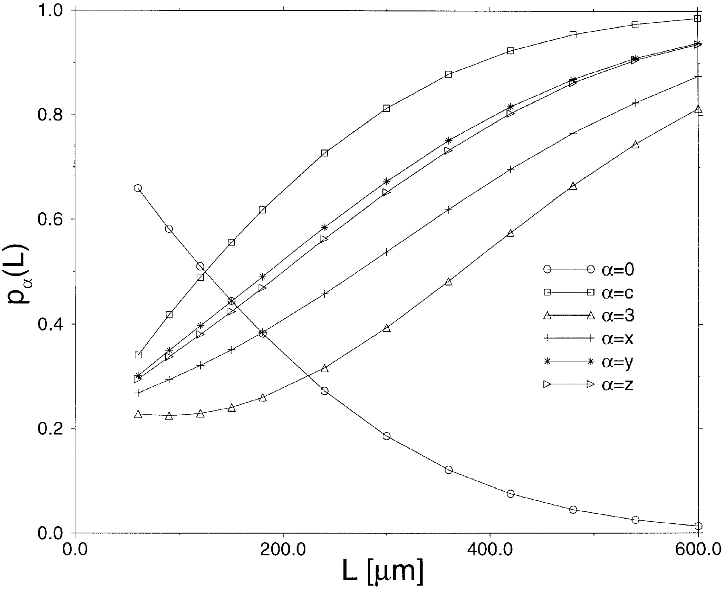

Fig. 13. Total fraction of percolating cells $p_\alpha(L)$ for the sandstone shown in Fig. 3.

and then carrying out the analysis on the remaining truncated sample. This did not produce differences between λ_x, λ_y and λ_z for sample A.

Hence, it must be concluded that sample C is anisotropic in its connectivity, being less permeable in the x-direction than in the y- and z-directions. We point out, however, that to the unaided eye Fig. 3 appears visually isotropic.

5. Comparison of results and discussion

Having presented the results for the various samples we now compare the samples against each other. Fig. 14 shows the local porosity distribution of all three samples at the same length $L = 120\,\mu\text{m}$. An important reason for the differences is different characteristic length scales for different samples. Sample C has clearly the largest length scale because its $\mu(\phi)$-curve is closest to the $L = 0$ limit of Eq. (2.4). Next comes sample A, and sample B has the smallest pores. The difference in characteristic length scales may be eliminated by comparing the samples at some intrinsic length scale such as the correlation length or the intrinsic length L^*.

Fig. 15 shows the comparison of all three samples at the intrinsic length $L = L^*$. Now, the local porosity distributions resemble each other much more closely. Nevertheless, characteristic differences remain not only in their peak position but also in their shape. These may in part, but not entirely, be attributed to the different porosities. Samples A and B have nearly the same porosities, but the shape of their $\mu(\phi, L^*)$ differs significantly. The width of the curves indicates the strength of porosity

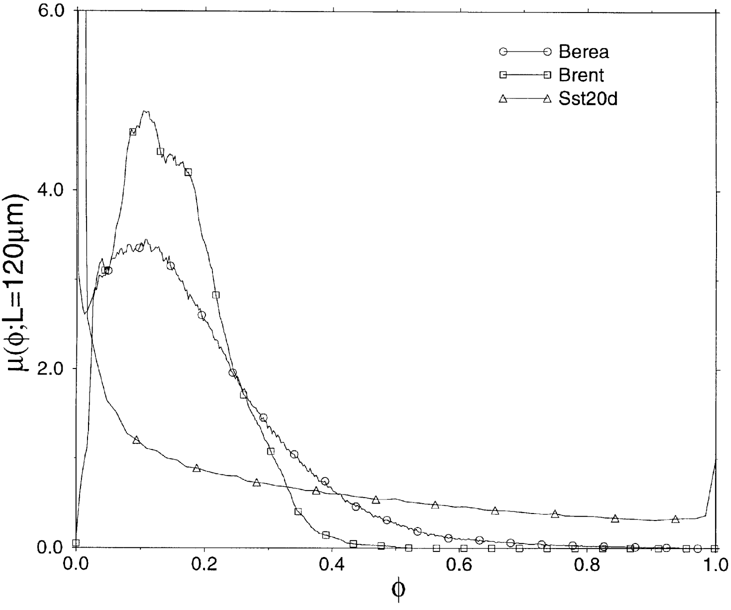

Fig. 14. Local porosity distributions $\mu(\phi, L = 120\,\mu\text{m})$ for all three samples.

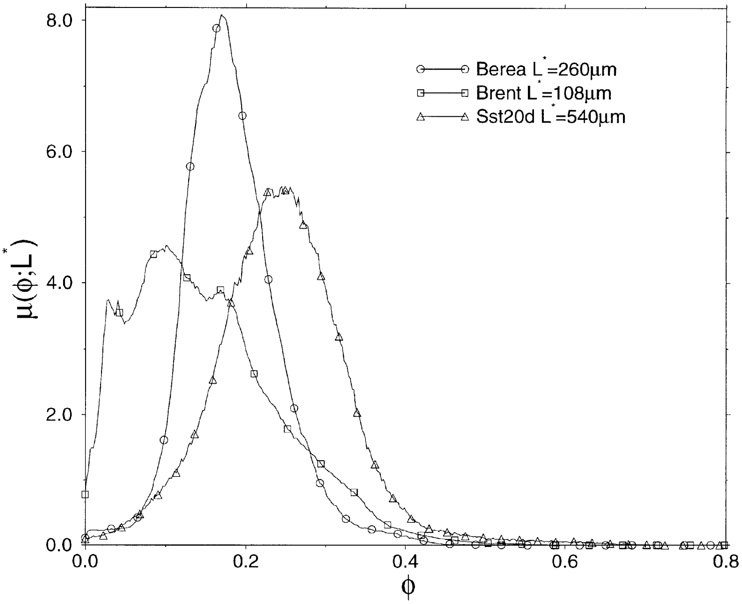

Fig. 15. Local porosity distributions $\mu(\phi, L = L^*)$ for all three samples.

fluctuations, and hence is a quantitative measure of heterogeneities in the porosity. Using the width as a criterion we find that sample A is most homogeneous while sample B is most heterogeneous, and sample C is intermediate. This agrees with visual inspection of Figs. 1–3, and illustrates that $\mu(\phi)$ measures porosity heterogeneities. This fact was first demonstrated for two-dimensional images in [13] and suggests the use of local porosity distributions and percolation probabilities as a quantitative method to compare microstructures between models and experiment.

In all three samples the behaviour of $\mu(\phi, L)$ as function of L seems to approach the limits given in Eqs. (2.4) and (2.6). This indicates that the samples approach macroscopic homogeneity for $L \to \infty$ [15]. Of course, much larger samples (particularly, for sample B) are needed to conclude this with certainty.

The behaviour of $\lambda(\phi, L)$ reflects the same trend towards macroscopic homogeneity because these functions approach a unit step at $\bar{\phi}$ with increasing L. The universality in the limit $L \to 0$ is reflected in the fact that the λ-curves for small L are very similar in Figs. 4, 8 and 11. This was already discussed above for $L = 4a$. Of course, for fixed L, the range of ϕ over which λ changes coincides with the range of ϕ where $\mu(\phi, L)$ differs from zero. Fig. 16 compares the local percolation probabilities λ_3 and λ_0 for all samples at $L = 120\,\mu$m. Not surprisingly the three samples exhibit very different behaviour analogous to the difference in μ seen in Fig. 14.

Fig. 17 shows λ_3 and λ_0 of all samples at the intrinsic length scale $L = L^*$. Characteristic differences in shape appear which emphasize the different connectivity of the three samples. These differences are not mere fluctuations because they are of the same order of magnitude as the differences introduced into λ_3 by the introduction of a

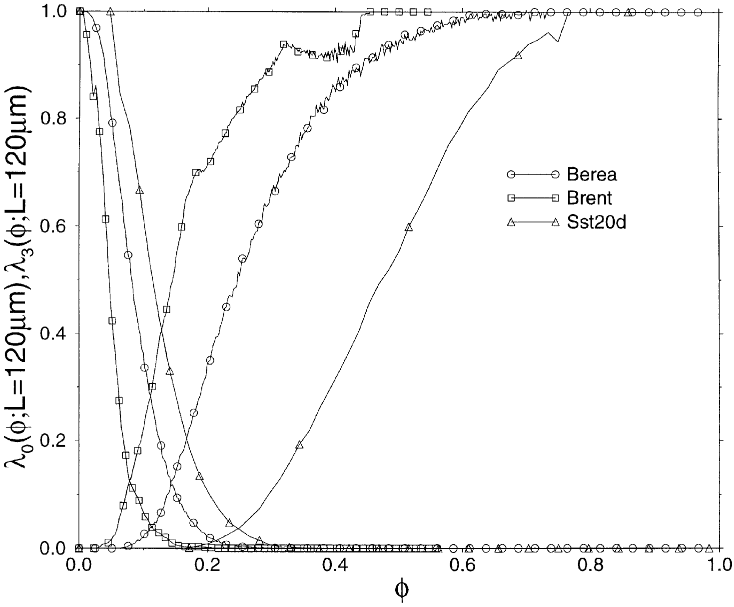

Fig. 16. Local percolation probabilities $\lambda_3(\phi, L=120\,\mu\text{m})$ and $\lambda_0(\phi, L=120\,\mu\text{m})$ for all three samples.

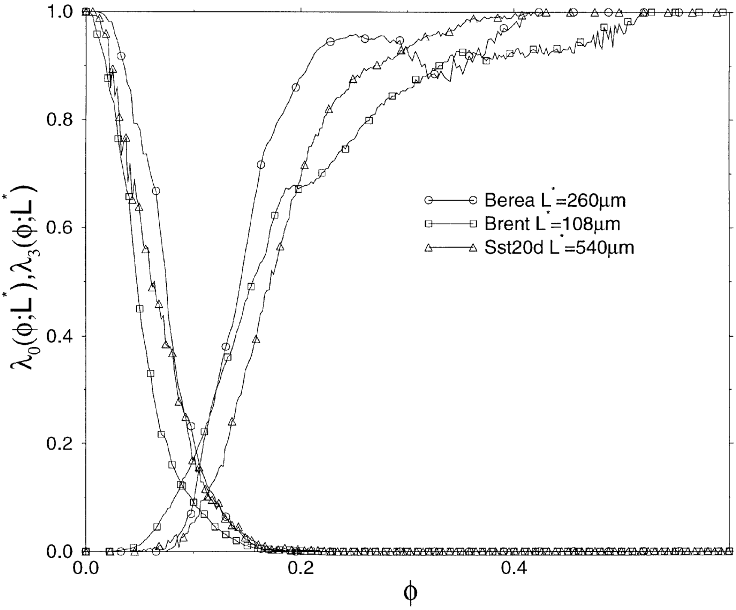

Fig. 17. Local percolation probabilities $\lambda_3(\phi, L=L^*)$ and $\lambda_0(\phi, L=L^*)$ for all three samples.

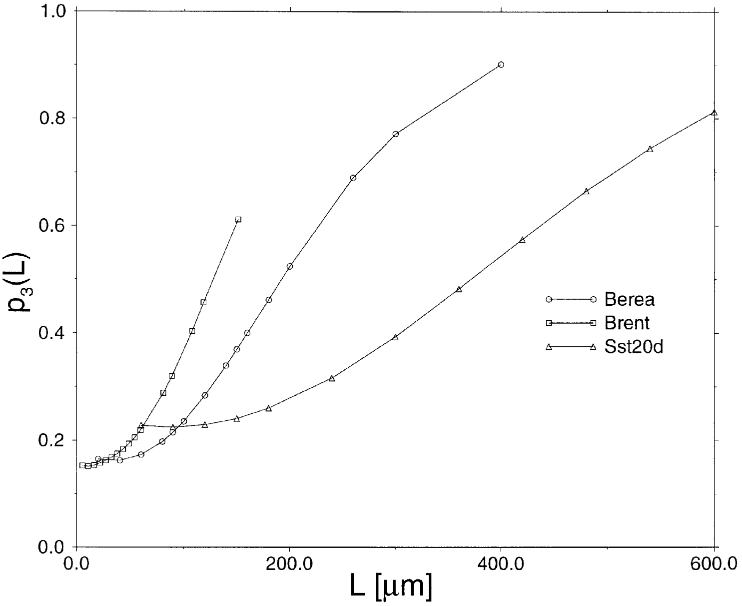

Fig. 18. Total fraction of percolating cells $p_3(L)$ for all three samples.

blocking plane into sample A that was discussed above. The curves are statistically most reliable for λ close to unity. This can be seen from Figs. 5, 9 and 12. These plots show that the maximum of μ occurs at ϕ-values for which λ is close to unity. They also show that the five functions λ_α with $\alpha = c, x, y, z, 3$ fall to the left of the maximum of μ for samples A and C, while for sample B these functions change most rapidly in the vicinity of the maximum of μ. Thus for samples A and C the change from blocking to percolating occurs well below the average porosity in the low porosity tail of μ, indicating that both samples have a very high degree of connectivity. The modified sample A (with partially blocking plane) shows a broader overlap between λ_α and μ indicating lower connectivity (see Fig. 6), and sample B appears to have the lowest degree of connectivity. In summary Fig. 17 shows that although all the samples are very well connected the fluctuations in connectivity are different, and hence one must also expect permeability fluctuations.

When comparing λ_3 for all samples it is seen that this function reaches a plateau at large ϕ. For sample A there is a region around $\phi \approx 0.3$ where λ_3 decreases (see Fig. 5). This shows that local percolation probabilities are not always strictly monotonous (as might have been expected) but may exhibit minima and maxima indicating a variable fraction of blocking cells and hence connectivity heterogeneities at intermediate scales.

Finally, it is instructive to compare the total fraction of percolating cells $p(L)$ for all samples. Figs. 7, 10 and 13 show that samples A and possibly B are essentially isotropic while sample C has clearly anisotropic connectivity. Fig. 18 shows $p_3(L)$ as calculated from Eq. (2.10) for all samples. This plot can be used for constructing network models in two ways. Firstly, if each $\mathbb{K}(\mathbf{x}, L)$ is used to represent a site in

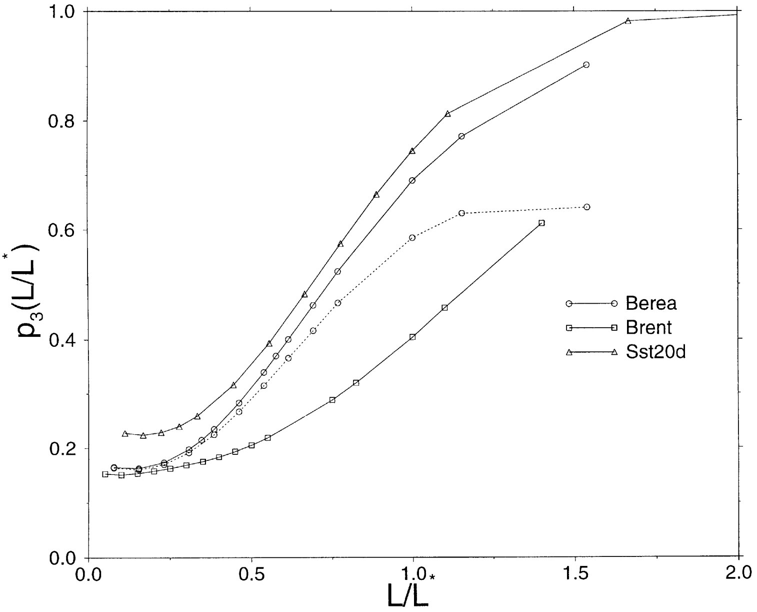

Fig. 19. Total fraction of percolating cells $p_3(L)$ for all three samples rescaled with L^*. The dotted line with circles is the result for the Berea sandstone (sample A) with a partially blocking yz-plane inside it.

the network model, $p_3(L)$ provides an estimate for the fraction of percolating network units as a function of the networks lattice constant. Secondly, $p_3(L)$ exhibits intrinsic length scales. Extrapolating a tangent at the inflection point of each curve to $p=1$ gives a length scale which could be interpreted as the minimum length scale for a representative elementary volume (REV) needed in homogenization and other averaging procedures [34,15]. In this way one finds approximately 350 μm for sample A, 230 μm for sample B and 700 μm for sample C as the smallest sidelength for an REV.

The results presented here suggest that none of the three samples can be adequately modelled by a critical site percolation network. The reason is that in such a model the fraction of percolating sites should equal p_3 and hence would be strongly L-dependent, except for very small or very large L. Hence, plots such as Fig. 18 or Fig. 19 provide information on how to choose the network elements (site, bonds) of a network model and how to relate the length scale of the real rock to the networks lattice constant.

Fig. 19 shows $p_3(L/L^*)$ for all samples as solid lines. The dotted line corresponds to the modified sample A with a partially blocking plane. The samples are again significantly different. The vertical shift is in part due to differences in porosity because generally $p_3(L=0)=\bar{\phi}$. The sample with the blocking plane indicates that it is possible to have intermediate plateaus and nonmonotonicity, at least if large-scale heterogeneities are present. The unmodified homogeneous samples exhibit different widths over which the curves increase from $\bar{\phi}$ to unity. These widths may be used as a quantitative measure of fluctuations in connectivity, both in theoretical models and in experiment.

Acknowledgements

The authors are grateful to Dr. P.E. Øren (Statoil), Dr. S. Bakke (Statoil), Dr. R. Hazlett (Mobil Exploration and Production) and Brookhaven National Laboratories for providing the sample data sets, and to the Deutsche Forschungsgemeinschaft for financial support.

References

[1] I. Fatt, The network model of porous media I. Capillary pressure characteristics, AIME Petroleum Trans. 207 (1956) 144.

[2] A. Scheidegger, The Physics of Flow Through Porous Media, University of Toronto Press, Toronto, 1974.

[3] I. Chatzis, F. Dullien, Modelling pore structure by 2-D and 3-D networks with applications to sandstones, J. Canadian Petroleum Technol. (1977) 97.

[4] J. Ziman, Models of Disorder, Cambridge University Press, Cambridge, 1982.

[5] J. Roberts, L. Schwartz, Grain consolidation and electrical conductivity in porous media, Phys. Rev. B 31 (1985) 5990.

[6] C. Jacquin, P. Adler, Fractal porous media II: Geometry of porous geological structures, Transport in Porous Media 2 (1987) 28.

[7] P. Adler, Porous Media, Butterworth-Heinemann, Boston, 1992.

[8] R. Blumenfeld, S. Torquato, Coarse graining procedure to generate and analyze heterogeneous materials: Theory, Phys. Rev. E 48 (1993) 4492.

[9] J. Feder, T. Jøssang, Fractal patterns in porous media flow, in: C. Barton, P.L. Pointe (Eds.), Fractals in Petroleum Geology and Earth Processes, Plenum Press, New York, 1995, p. 179.

[10] D. Jeulin, A.L. Coënt, Morphological modeling of random composites, in: K. Markov (Ed.), Continuum Models and Discrete Systems, World Scientific, Singapore, 1996, p. 199.

[11] J. Andrade, M. Almeida, J.M. Filho, S. Havlin, B. Suki, H. Stanley, Fluid flow through porous media: The role of stagnant zones, Phys. Rev. Lett. 79 (1997) 3901.

[12] P. Øren, S. Bakke, O. Arntzen, Extending predictive capabilities to network models, SPE Proc. SPE 38880, 1997 (1997) 369.

[13] F. Boger, J. Feder, R. Hilfer, T. Jøssang, Microstructural sensitivity of local porosity distributions, Physica A 187 (1992) 55.

[14] C. Andraud, A. Beghdadi, J. Lafait, Entropic analysis of random morphologies, Physica A 207 (1994) 208.

[15] R. Hilfer, Transport and relaxation phenomena in porous media, Adv. Chem. Phys. XCII (1996) 299.

[16] C. Andraud, A. Beghdadi, E. Haslund, R. Hilfer, J. Lafait, B. Virgin, Local entropy characterization of correlated random microstructures, Physica A 235 (1997) 307.

[17] C. van Siclen, Information entropy of complex structures, Phys. Rev. E 56 (1997) 5211.

[18] J. Quiblier, A new three dimensional modeling technique for studying porous media, J. Colloid Interface Sci. 98 (1984) 84.

[19] C. Yeong, S. Torquato, Reconstructing random media, Phys. Rev. E 57 (1998) 495.

[20] U. Oxaal, F. Boger, J. Feder, T. Jøssang, P. Meakin, A. Aharony, Viscous fingering in square lattice models with two types of bonds, Phys. Rev. A 44 (1991) 6564.

[21] M. Blunt, M. King, H. Scher, Simulation and theory of two-phase flow in porous media, Phys. Rev. A 46 (1992) 7680.

[22] G. Stell, Mayer-montroll equations (and some variants) through history for fun and profit, in: M. Shlesinger, G. Weiss (Eds.), The Wonderful World of Stochastics, Elsevier, Amsterdam, 1985, p. 127.

[23] F. Dullien, Porous Media – Fluid Transport and Pore Structure, Academic Press, San Diego, 1992.

[24] S. Bakke, P. Øren, 3-D pore-scale modelling of heterogeneous sandstone reservoir rocks and quantitative analysis of the architecture, geometry and spatial continuity of the pore network, SPE Proceedings, SPE 35479, vol. European 3-D Reservoir Modelling Conference, Stavanger, Norway, 1996.

[25] R. Hilfer, Geometric and dielectric characterization of porous media, Phys. Rev. B 44 (1991) 60.
[26] R. Hilfer, Local porosity theory for flow in porous media, Phys. Rev. B 45 (1992) 7115.
[27] R. Hilfer, Geometry, dielectric response and scaling in porous media, Phys. Scripta T44 (1992) 51.
[28] R. Hilfer, Local porosity theory for electrical and hydrodynamical transport through porous media, Physica A 194 (1993) 406.
[29] B. Hansen, E. Haslund, R. Hilfer, B. Nøst, Dielectric dispersion measurements of salt water saturated porous glass compared with local porosity theory, Mater. Res. Soc. Proc. 290 (1993) 185.
[30] R. Hilfer, B. Nøst, E. Haslund, Th. Kautzsch, B. Virgin, B.D. Hansen, Local porosity theory for the frequency dependent dielectric function of porous rocks and polymer blends, Physica A 207 (1994) 19.
[31] B. Virgin, E. Haslund, R. Hilfer, Rescaling relations between two- and three dimensional local porosity distributions for natural and artificial porous media, Physica A 232 (1996) 1.
[32] S. Bakke, P. Øren, private communication.
[33] D. Stauffer, A. Aharony, Introduction to Percolation Theory, Taylor and Francis, London, 1992.
[34] J. Bear, Y. Bachmat, Introduction to Modeling of Transport Phenomena in Porous Media, Kluwer Academic Publishers, Dordrecht, 1990.
[35] B. Biswal et al., to be published.